FINAL REPORT

Compound Refractive Lenses for Thermal Neutron Applications

Adelphi Technology, Inc.
2003 E Bayshore Rd
Redwood City, CA 94063

PI: Dr Charles K Gary
Topic: 13a
Grant #: DE-FG02-08ER84991

We designed, constructed and tested thermal neutron lenses in this contract. These lenses, made from Teflon AF 1600, demonstrated improved focal lengths, fields of view, surface quality, material homogeneity and radii of curvature. Most importantly, we demonstrated the use of a molding technique to fabricate these lenses that can be easily applied to the production of Fresnel lens designs. A summary of the achievements under each goal of the research plan follows.

Goal 1. Analysis of CRLs

We considered a number of lens materials in addition to the Teflon AF 1600 that we used for our Phase I prototype. Probably the most important parameter for any neutron lens material is the ratio of δ/μ, which determines the maximum numerical aperture, and hence the relative resolution and efficiency that can be achieved. Aluminum offers better performance, but cannot be as easily formed as Teflon. Other materials are both harder to work with and offer lower performance. MgF_2 is a popular material for neutron CRLs due to the availability of off-the-shelf lenses made for visible light optics and its single crystal structure that limits scattering. However, these lenses tend to have radii of curvature 1 mm or greater and are not easily formed into smaller radii or Fresnel shapes. We have avoided the scattering problems by using amorphous Teflon AF 1600. While this material is relatively expensive at over $40/gram, only small quantities are required, so that material costs are less than the machining and molding. We will continue to consider aluminum, including Fresnel designs, in Phase II.

Material	δ at 1.8 Å	μ at 1.8 Å (cm^{-1})	δ/μ at 1.8 Å (cm^{-1})
Aluminum	$1.07x10^{-6}$	0.10	$1.03x10^{-5}$
C_2F_4 (Teflon)	$1.98x10^{-6}$	0.21*	$9.43x10^{-6}$
Magnesium	$1.19x10^{-6}$	0.16	$7.34x10^{-6}$
MgF_2	$2.64x10^{-6}$	0.36	$7.26x10^{-6}$
Carbon	$3.88x10^{-6}$	0.63	$6.17x10^{-6}$
Beryllium	$4.96x10^{-6}$	0.94	$5.26x10^{-6}$
Bismuth	$1.24x10^{-6}$	0.26	$4.79x10^{-6}$
Iron	$4.13x10^{-6}$	1.20	$3.44x10^{-6}$
Copper	$3.37x10^{-6}$	1.00	$3.37x10^{-6}$
Nickel	$4.85x10^{-6}$	2.10	$2.31x10^{-6}$

Table I. Lens material figures of merit. Data from the NIST NCNR database, *except for the μ for Teflon, which is based on our measurements. The NCNR value is 0.25 cm^{-1}.

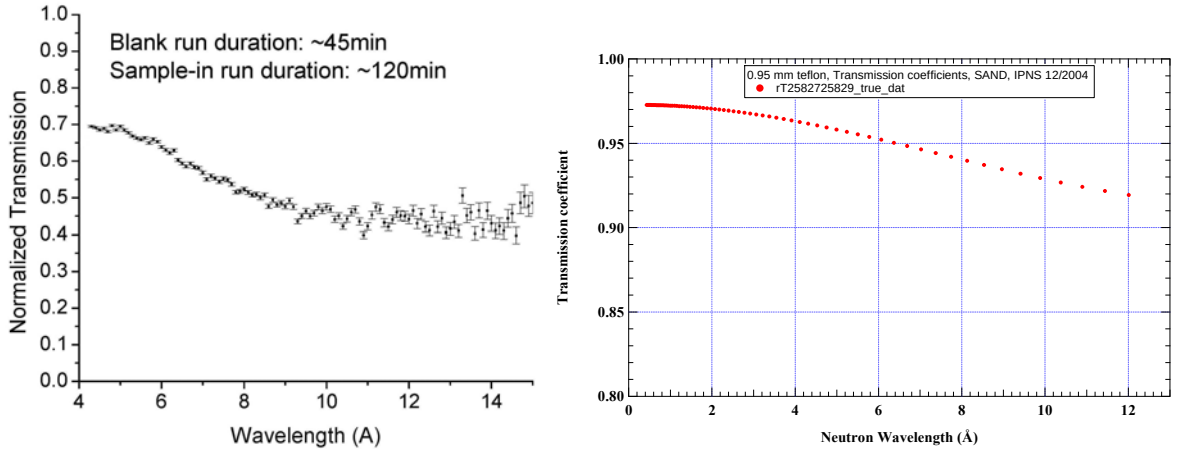

Fig. 4. Measured absorption in a 12 mm Teflon AF sample. Transmission is the ratio of the signal at each wavelength without and with the sample in the beam.

The quality of the scattering data is important to the analysis of materials. We used the Computer Index of Neutron Data (CINDA), which can be found at http://www.nndc.bnl.gov/nndc/cinda/ , the T-2 database at Los Alamos National Laboratory (t2.lanl.gov) and the NIST Center for Neutron Research (NCNR), http://www.ncnr.nist.gov/resources/n-lengths/. However, there remains some question of the

scattering data for Teflon and how this relates to the performance of amorphous Teflon. The tabulated data is for pure elements. The databases provide cross sections for coherent scattering, incoherent scattering, and thermal neutron absorption for both C and F, though the NCNR only has values at 1.8 Å. We obtained the Teflon linear attenuation by adding the respective products of the cross section and number density for carbon and fluorine in Teflon. Using a density of 1.78 g/cm3, the calculated absorption constants, μ, are given in Fig. 5. The coherent scattering cross section (5.6 barns for C and 4.0 barns for F at 1.8 Å) dominates the other cross sections (all less than 10 mbarns). Unfortunately, it is not clear what percentage of the coherent scattering cross section is due to elastic vs. inelastic scattering, which is critical since elastic scattering contributes to refraction but not loss. Also, neutron scattering is highly dependent on local density variations and crystalline structures. Indeed, we chose amorphous Teflon to avoid scattering from microcrystals, but the effect of crystal structure and density variations on the tabulated data is unknown.

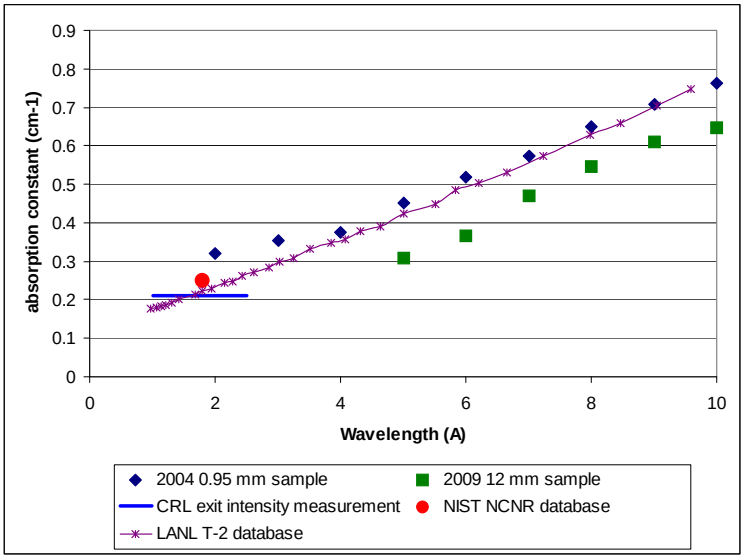

Fig. 5. Theoretical and measured absorption coefficients for Teflon.

To get a better understanding of the scattering in amorphous Teflon AF, we made several measurements. At the Low Energy Neutron Source (LENS) at Indiana University, we measured the transmission as a function through our CRL. At LENS, Roger Pynn, our consultant, was able to measure the transmission at wavelengths from 4-14 Å. Unfortunately, the facility at LENS was not designed for thermal neutron production and could not measure wavelengths shorter than 4 Å. The measured absorption in a 12 mm thick sample is shown in Fig. 4a Prof. Pynn was also able to provide data taken previously with a 0.95 mm thick Teflon sample, though its quality is unknown. This data is also given in Fig. 4b. Unfortunately, the transmission approached an asymptote at a transmission of 0.97 rather than 1. Prof. Pynn believes that this may have been due to scattering from the front and back surfaces of the material. These effects would not be as significant for the more absorbing 12 mm sample; thus we believe that the 12 mm data is more reliable, but the 0.95 curve can be used to extrapolate the 12 mm data to shorter wavelengths. We also measured the relative absorption vs. radial distance at the exit of our Phase I Teflon NCRL. This measures the average absorption over the full bandwidth of the Maxwell-Boltzmann spectrum of the beam and is distorted by the bending of rays in the lens, but gives a general indication of the absorption constant. This measurement gives a value of 0.21 cm^{-1}, which corresponds well to an extrapolation from the 12-*mm* sample data. The values from these various measurements and the tabulated value(s) are given in Fig. 5. Based on these measurements, we have decided to use the measured value of 0.21 cm^{-1} for our calculations of future designs.

We also considered surface roughness. As stated in the Phase I proposal, to avoid significant scattering requires the rms roughness σ to be:

$$\sigma < \lambda / 4\delta\sqrt{2N} \qquad (6)$$

Note that the required roughness is reduced by the square root of the number of lenses. Thus, the roughness is on the order of visible optics lenses. For example, for the Teflon lens we tested, with $N = 78$ unit lenses, $\delta = 2.4 \times 10^{-6}$ at $\lambda = 1.8$ Å, then $\sigma < 1.5$ μm, which is less strict than that for visible light. Thus, we used the response of the lenses to visible light to judge their quality under goal 2 with the understanding that mildly flawed lenses would probably still provide accurate focusing for neutrons.

In our Phase I proposal we presented both theory and experiment to show that the performance of spherical and parabolic CRLs would be equivalent for neutron beams with bandwidths of 2% or larger. We also did all our Phase I experimental work on a broadband beamline at MNRC. However, we chose to fabricate parabolic lenses for several reasons. First, the number of unit lenses required is inversely proportional to the radius of curvature of the lens, but the maximum aperture of a spherical unit lens is twice the radius of curvature. For the 187-μm radius lenses we made, the maximum aperture would have been 375 μm, whereas we manufactured lenses with a physical aperture of 3 mm. Second, we plan to use these lenses on monochromatic beamlines, such as those available at LANSCE and NIST, where the optimum achievable resolution could be degraded by the spherical shape. Third, we want to test our ability to mold shapes with a steep, parabolic slope, as this is required for the production of Fresnel lenses.

Goal 2. Fabricate molded coin lenses using Teflon AF. Fabricate bubble lenses using Teflon AF.

We fabricated parabolic compound neutron lenses from Teflon using a "coin" molding technique that we originally developed for x-ray optics made from plastic. Individual unit lenses for the compound lens were made by injection molding the Teflon using a diamond turned parabolic master. For x-ray lenses, the parabola only extends a fraction of a millimeter into the substrate, giving the appearance of a coin with a small indentation, hence the name. Because the absorption and index of refraction are much smaller for thermal neutrons than for x rays, the parabola for the unit neutron lenses extend as much as 6 mm, creating a shape more like a drinking glass than a coin as can be seen in Fig. 6. We chose to fabricate plano-concave rather than bi-concave lenses due to the easier manufacture; only one parabolic master needed to be made, and fewer elements needed to be aligned in the mold.

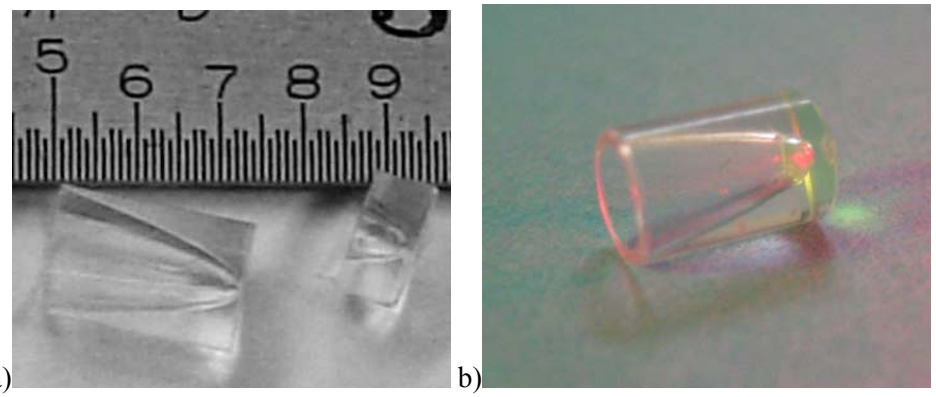

Fig. 6. Photographs of 6-mm long Teflon AF 1600 unit lenses. Each lens had a 4-mm outer diameter and a parabolic radius of curvature of 187 μm.

To injection mold the lenses, we require a material that can be heated to flow, but cools to a solid. Amorphous fluoropolymer resin (Teflon) is an ideal such substance for neutrons since it contains only F and C molecules. Our chosen resin (Teflon AF 1600 by DuPont) already has applications as a visible optics lens because of its transparency and excellent surface quality, which result from its amorphous structure. The typical molding temperatures of 240ºC to 275ºC for this Teflon allow it to be injection and compression molded into most any shape, including plano-concave parabolic neutron lenses. Teflon AF is expensive, selling for approximately $40/g, however, large quantities are not required. The 78-element compound lens built and tested used approximately 6 g. The injection molding was performed under subcontract to Random Technologies of San Francisco, which possesses the necessary injection molding equipment and license from DuPont and has extensive experience in the use of amorphous Teflon.

We had 100 parabolic lenses fabricated out of Teflon AF 1600 in order to construct a low absorption compound refractive lens for use with thermal neutrons. Although Random Technologies has previously molded optical parts using Teflon AF 1600, the construction of such a deep concave parabolic lens of the type we requested was new territory for them. The molding process would produce occlusions or distorted shapes in some of the unit lenses, necessitating a quality control process to select the best unit lenses.

The very deep concave parabolic shape of the lenses is very difficult to fully test nondestructively. The testing method decided upon was a qualitative test due to the intrinsic difficulty of testing the lenses and the time constraints between lens delivery and experiment at the reactor facility. The lenses were tested using a high NA focusing lens illuminated by a large diameter, collimated HeNe beam. The focusing probe beam was directed into the plano end of the Teflon lens. This configuration is similar to what is known as a Galilean telescope. In this configuration ideally the converging beam will be collimated by the concave, parabolic lens. Because the converging probe beam has a high NA, the plano surface will distort much of the beam before it encounters the concave, parabolic surface. Much of the beam that exits the test lens will, therefore, not be collimated. The central part of the beam (of low NA) will be collimated.

The qualitative testing focused on two aspects of the appearance of the beam exiting the test lens.

1. Was the small collimated beam from the central, low NA, portion of the probe beam of high intensity? That would determine the percentage of the point of the parabola that was well formed. Unit lenses were given a rank of: I1, I2, and I3 – I1 being the most intense collimated beam. It was expected that this part of the lens would be the most important in determining the image quality because of its lower absorption being near the point of minimum lens center thickness.

2. Was the "flare light" around the collimated beam of even intensity? This was the probe light that did not collimate because of the aberration introduced by a high NA light beam entering the parabolic lens after going through a plano surface. This exit beam pattern was given a rank of: M1, M2, and M3 – M1 being the pattern with the most even intensity distribution.

When it came time to assemble the 78 element compound refractive lens system it was necessary to include not only I1's, M1's but also I2's and M2's. However, the performance of the lenses is more tolerant of surface errors for neutrons than visible light. It should be noted that the figure error of the lens, which we have not yet measured probably contributes more to distortion at this point than the surface quality. We measure and thus control the figure error in Phase II.

There is no intrinsic reason that in the future much better lenses cannot routinely be produced by an injection molding process. The major molding problem with all thermoplastics is shrinkage, and this was the case with the parabolic lenses delivered.

We also explored the production of Teflon CRLs using a bubble lens technique previously used at Adelphi for x-ray optics. For x rays, bubble lenses are made by wicking epoxy into a capillary (e.g., inside diameter 200 μm, ouside 5 mm). The capillary is placed on a stepper-motor-driven translation stage. A hypodermic needle is insered into the capillary. Air is injected into the needle and the translation stage is moved at an accelerated rate. Bubbles form if the gas pressure and rate of translation are in a given parameter range. However, we were not able to achieve the needed viscosity of the Teflon to produce quality lenses. In addition, this technique produces spherical lenses and does not provide a manufacturing path for the production of Fresnel lenses, which is important to our Phase II work. Thus, we decided to concentrate on the production of molded lenses.

Goal 3. Test the CRLs fabricated under goal 2

We measured the resolution, transmission, field of view (FOV), and wavelength range of the Teflon CRL on beam line 4 at the McClellan Nuclear Radiation Center (MNRC) in Davis, California. The MNRC wavelength spectrum is a Maxwell-Boltzmann distribution with a peak at 1.2 Å. Thermal neutrons from the reactor water core pass through a graphite moderator and 28-*cm* long sapphire crystal, which improves the thermal content by reducing the

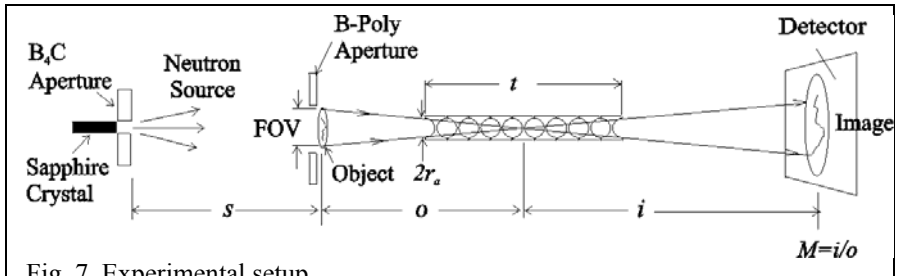

Fig. 7. Experimental setup.

relative number of higher energy neutrons. The neutrons emerge from a 3.2-*cm* square aperture in a boron carbide shielding plate. Thus, the effective source size is a 3.2-*cm* square. The neutrons from the reactor emerge into the experimental chamber 3.0 *m* downstream through a 2.5-*cm* aperture in a 2.5-*cm* thick lithium enriched polyethylene shield with a 1-*mm* Cd layer. The shield reduces the radiation from stray neutrons. The thermal neutron flux at the shield aperture was 1.7×10^6 $n/cm^2 \cdot s$.

The detector used for the measurements was a FCR XG-1NDT Fuji-film system based on photo-stimulated luminescence. The imaging plate (IP) consists of a photostimulable phosphor layer with a gadolinium-based converter material and photo-stimulated luminescence material. The converter absorbs neutrons and emits secondary radiation, and this secondary radiation is detected by the photo stimulable storage phosphor. If an area of the photostimulable phosphor has previously been exposed to radiation, it will emit light when interrogated by a laser. The laser spot size, grain size in the phosphor, and scanning rate yield a specified resolution of ~100 μm pixels, or a spatial frequency of 3.3 mm^{-1}. The imaging plate is 23 cm x 25 cm in area.

Resolution

The resolution was measured by imaging a series of Cd grids. The experimental setup is shown in Fig. 7. The object to be imaged was placed as close as possible to the source, about 4.3 m for Bay 4. The CRL and detector were then placed to satisfy the lens equation. At 1.95 Å and a magnification of 2, this yields an object to CRL distance, *o*, of 1.62 *m* and a CRL-to-detector distance, *i*, of 3.24 *m*. The object was placed at the center of the 2.5-*cm* aperture in the shield, while the CRL and detector were mounted on an optical rail. The beamline at Bay 4 is inclined at a 22º angle. The CRL holder, and thus the CRL, was aligned to the neutron beam using a pre-aligned laser provided by MNRC. The slits were formed in a 2.5-*cm* x 5-*cm* x 0.5-*mm* Cd sheet. The length of the slits was 1 *cm* and the width varied from 2.54 *mm* to0.20 *mm*, with the spacing between slits equal to the width.

Images were taken of 2.54, 1.27, 0.63,0.38 and

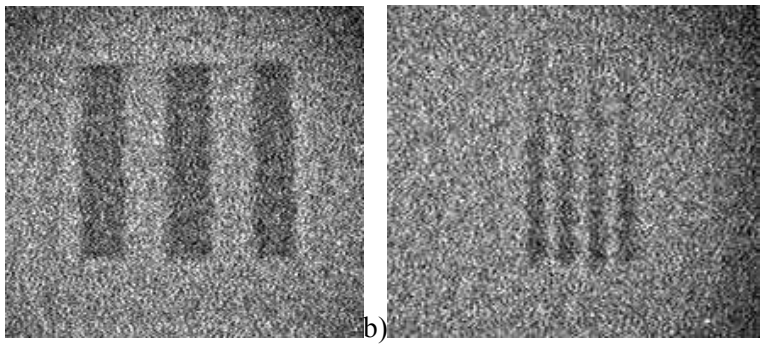

a) b)

Fig. 8 Neutron image of (a) 1.27-mm and (b) 0.38-mm slits in 0.5-mm thick Cd. The edge of the field of view can be seen at the top of the 0.38-mm slits. The CRL was located to image 1.95 Å neutrons with no filtering of the Maxwellian neutron spectrum. Images were acquired in 3 hours using a phosphor plate and film detector.

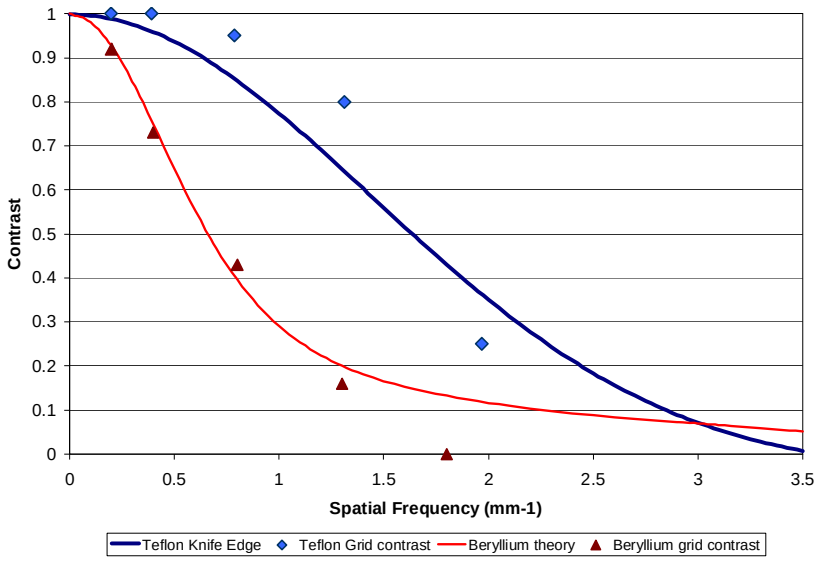

Fig. 9. Grid contrast measurements and calculated MTFs for a 78 element Teflon AF1600 NCRL (R=187μm) and 155 element Be NCRL (R=2mm) at λ=1.95Å

0.25-*mm* slit arrays. The images of the 1.27 and 0.38-*mm* slits are shown in Fig. 8. The exposure time was 3 hours. This long time was required due to the inefficiency of the imaging plate and the low neutron flux on this beamline. We used two methods to calculate the resolution. We measured the contrast between dark and light regions of the images, representing the presence and absence of neutrons from the slits for varying slit widths (spatial frequencies). We also calculated the modulation transfer function from the sharpness of the transition from the dark to light regions of the image called "knife edges". This provides a measure of the CRL's resolution, though convolved with the detector and the sharpness of the edges in the Cd slits. The results of these measurements and calculations are given in Fig. 9, and the edge response to MTF calculation is explained below. We could easily resolve the 0.25-*mm* slits, and the MTF of 0.15 (the Rayleigh criterion) also indicates a resolution of 2.5 *lp/mm* or 200 μm.

The MTF can be calculated from the edge response, as follows. The ***K(x)***= the measured knife edge response is given by

$$K(x) \propto \int_{-\infty}^{x} d\gamma \int_{-\infty}^{\infty} d\eta PSF(\sqrt{\gamma^2+\eta^2}) \tag{7}$$

where *PSF(u)* = the point spread function of the imaging system and *u*= the coordinate in the object plane

The line spread function, *LSF*, is

$$LSF(\gamma) = \int_{-\infty}^{\infty} d\eta PSF(\sqrt{\gamma^2+\eta^2}) \tag{8}$$

so that

$$K(x) \propto \int_{-\infty}^{x} d\gamma LSF(\gamma) \tag{9}$$

The MTF is the normalized Fourier transform of the LSF

$$MTF(p) = \frac{\int_{-\infty}^{\infty} d\gamma LSF(\gamma) Cos\frac{2\pi\gamma}{p}}{\int_{-\infty}^{\infty} d\gamma LSF(\gamma)} \tag{10}$$

From (9),

$$\frac{dK(x)}{dx} \propto LSF(x) \tag{11}$$

Thus,

$$MTF(p) = \frac{\int_{-\infty}^{\infty} d\gamma \frac{dK(\gamma)}{d\gamma} Cos\frac{2\pi\gamma}{p}}{\int_{-\infty}^{\infty} d\gamma \frac{dK(\gamma)}{d\gamma}} \tag{12}$$

The MTF is the Fourier transform of the derivative of the knife edge function. Since $\frac{dK(\gamma)}{d\gamma}$ approaches zero near the edge, the limits in Eq.(6) can be replaced with finite limits. Integrating Eq.(12) by parts

$$MTF(p) = \frac{K(b)Cos(\frac{2\pi b}{p}) - K(a)Cos(\frac{2\pi a}{p}) + \frac{2\pi}{p}\int_{a}^{b} d\gamma K(\gamma) Sin(\frac{2\pi\gamma}{p})}{K(b)-K(a)} \tag{13}$$

where *a* and *b* are the limits of integration. The knife edge measurement may be normalized so that *K(b)*=1 and *K(a)*=0, whereupon Eq.(13) becomes

$$MTF(p) = Cos(\frac{2\pi b}{p}) + \frac{2\pi}{p}\int_a^b d\gamma K(\gamma) Sin(\frac{2\pi\gamma}{p}) \quad (14)$$

Equation (12) or (14) may be used to obtain the MTF from the measured knife edge data.

Figure 9 gives the results of these resolution measurements. The knife edges were calculated from the edges observed on a 1.27-*mm* grid. The individual data points are the measured contrast for a range of grids. Also plotted in the graph are the theoretical MTF and the measured contrast from grids for a 155 element, R=1.98 *mm* beryllium CRL that had the best resolution we previously measured for thermal neutrons. Thus, the Teflon NCRL has outperformed all previous thermal NCRLs.

Field of View

In the imaging experiments described above, the field of view (FOV) was limited by the size of the neutron source. In order for a point on the object to be seen, rays from the source must pass through the object and then strike the lens. The angle subtended by the sapphire crystal source as seen from the lens $D_{source}/(s+o)$ = 5.3 mradians or about 7.5 mm for 2X magnification at 1.95 Å. The FOV of the Teflon CRL is larger and is determined by the angle at which neutrons are absorbed in the lens. Taking the absorption aperture as the effective aperture of the CRL, the FOV is limited by the angle of rays that pass through the non-absorbing portion of the unit lenses, which is given by L/d, where L is the CRL length and d the aperture diameter. To test the FOV, we cut the unit lenses down to approximately 2 mm in length each, giving a total CRL length of 180 mm. An absorption aperture of 1.5 mm, gives a FOV of 17 mradians. Since we could not move the source within the nuclear reactor to test the FOV, we measured it by tilting the CRL. With sufficient tilt, neutrons from the source would travel through absorbing portions of the CRL. Note that the CRL aperture does not have a hard cutoff at the absorption aperture, but rather just continually increasing absorption. Thus, the map of intensity vs. tilt (or view angle) falls off gradually. Since the FOV extends to both sides of the optical axis, it is equal to twice the limiting view angle, or approximately 40 mradians. This is even larger than predicted from the absorption aperture; however, based on our extensive absorption measurements, we feel confident in the absorption aperture.

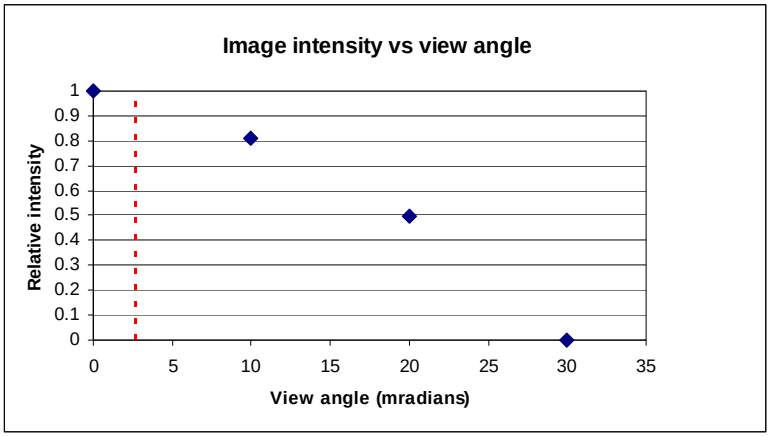

Fig. 10. Relative intensity vs. view angle for 1.27 mm grids imaged at 2X magnification at 1.8 Å. The effective FOV is twice the view angle; thus the FOV for 50% intensity would be 40 mradians. The vertical red line indicates the limit to the FOV caused by the small source size.

Spectrum measurement – operational wavelengths

Given the long focal lengths at higher energies and the limited experimental distance in Bay 4, we could not image grids below about 1.7 Å. However, we were able to test the ability of the CRL to image at various wavelengths by imaging the sapphire crystal source (Fig. 7). To do this we placed the NCRL at a point 5 *m* from the sapphire crystal and varied the position of the IP plate detector to capture images of the source at various wavelengths. Using the lens equation, the object distance (source to lens in this case) and the image distance (lens to detector) determine the focal length. The wavelength can then be calculated from $\delta(\lambda)$. Fig. 11(a) shows the image of the source at 1.61 Å. The shortest wavelength we were able to image at was 1.26 Å. By integrating the total flux over the area of the square image of the

source, we were able to estimate the intensity spectrum of the source. For these measurements, it was important to subtract the background exposure due to gamma radiation and scattered neutrons. Unfortunately, for our measurements at 1.26 and 1.34 Å, the image was sufficiently large to significantly

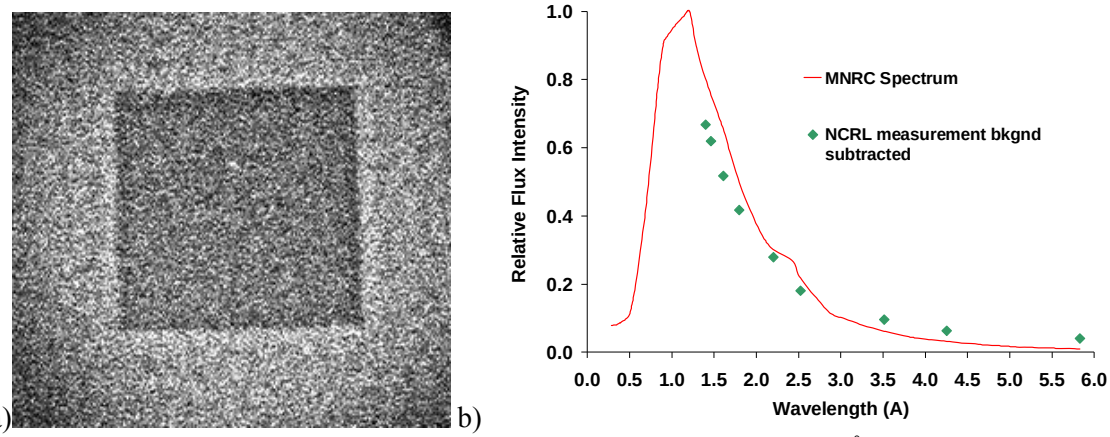

Fig. 11. a) Image of the sapphire crystal neutron source at MNRC taken at 1.61 Å. b) plot of the relative flux measured in the square image of the source vs. wavelength and the MNRC spectrum.

overlap regions with very intense gamma backgrounds. In addition, the lower magnification at short wavelengths left the energy from the beam distributed over a larger area, making the subtraction increasingly difficult at short wavelengths, despite the increased intensity of the beam. Thus, we were only able to get reliable quantitative data at 1.4 Å and longer wavelengths as shown in Fig. 11(b).

Goal 4. Design Fresnel CRLs

CRLs have a limited aperture due to material absorption as given by eq. (4). One means of overcoming the limited absorption aperture of CRLs is to use a Fresnel lens shape. Fig.12 depicts how a parabolic refractive lens is conceptually converted to a refractive Fresnel lens. Only the material interfaces of the Fresnel segments deflect and focus the neutrons. The absorbing segment behind the refractive segment is of no use and results in increased neutron absorption. Removing material in steps does not interfere with the lens' ability to refract the neutrons. Since the Fresnel lens can be thin and its surface follows a parabolic shape in steps, the refractive Fresnel lens can achieve a larger clear aperture. Fresnel lenses are used for visible optics when a thin lens is needed. Lens performance characteristics that improve with a Fresnel lens are:

- Increased aperture.
- Increased image intensity.
- Better resolution.
- Higher beam transmission.
- Larger field of view, a consequence of a larger aperture.

We have developed models to calculate the performance of Fresnel CRLs and determine the

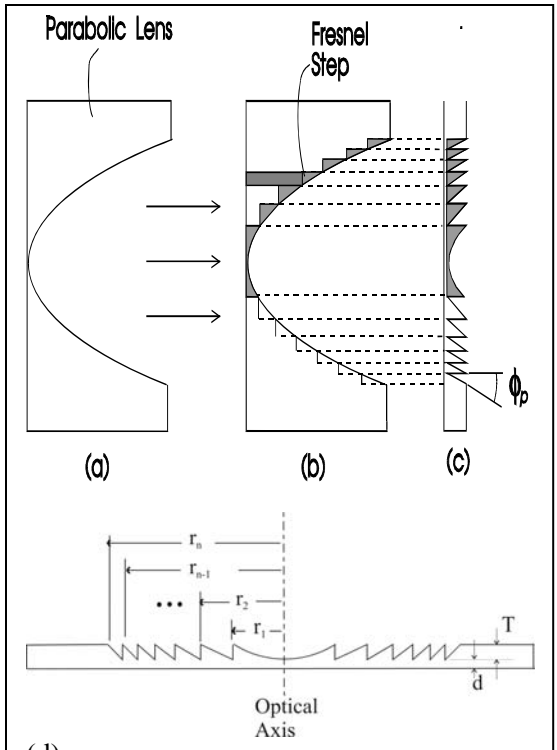

Fig. 12. Diagram of the construction of a Fresnel lens. (a-c) show the process and (d) shows the parameter of the resulting lens.

necessary manufacturing precision, alignment, etc. For the Fresnel lens, the steps are placed such that the power absorption is reduced by the factor e^{-a}, where $a = \mu NT$, with $T = \frac{1}{2R}\left(r_n^2 - r_{n-1}^2\right)$ being the thickness of the unit lens, N the number of unit lenses, and μ the power absorption constant. With this condition, the step locations, r_n, are given by

$$r_n = \sqrt{2RnT} = \sqrt{\frac{2Rna}{N\mu}} = A\sqrt{\frac{na}{8}} \tag{15}$$

where, $A = 4\sqrt{f\delta/\mu} = 4\sqrt{R/N\mu}$ is the absorption aperture for plano-convex parabolic CRLs. Due to the absorption in neutron optics, the analyses developed for visible light are not readily applicable, and we have developed our own calculations of the lens performance starting from the Kirchoff equation., which yields the intensity at an image point from a point in the object plane. Since neutron trajectories must satisfy the lens condition to contribute to the image, the Kirchoff equation becomes

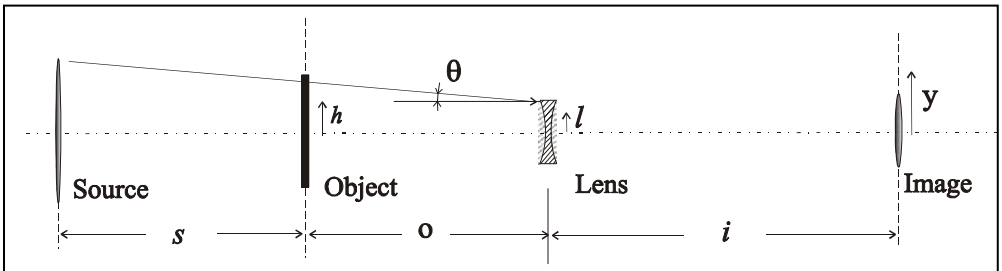

Fig. 13. Optical layout of neutron imaging system, including parameters used for Kirchoff calculations.

$$I \propto \int_{-\infty}^{\infty} d\lambda g\{\lambda\} \left| \int_{-\infty}^{\infty} dl Exp\left\{ \left(ik2N\delta(\lambda) - N\mu(\lambda)\right) * t\{l\} + ikp\left(\frac{h}{o} + \frac{y}{i} - \frac{l}{2f}\right)\right\}\right|^2 \tag{16}$$

where g(λ) is the neutron spectrum, *t(l)* the shape of the lens, and *s, h, o, y, i, l* are shown in Fig.13. Critical to the performance of the Fresnel CRL is its point spread function (PSF), which is equivalent to its impulse response. We can calculate the PSF from the Kirchoff equation. For a polychromatic source with random phase shift between zones, the PSF for a Fresnel lens referred to the object coordinate, r_1 is

$$PSF(r_1) \propto \int d\lambda \frac{g(\lambda)}{\lambda^2} Exp[-\mu(\lambda)Nb] \sum_{n=0}^{Z-1} \left| Exp\left[\frac{na}{2}\right] \int_{\sqrt{\frac{2Rna}{N\mu}}}^{\sqrt{\frac{2R(n+1)a}{N\mu}}} rdrJ_0\left(\frac{kr_1 r}{q}\right) Exp\left[-j\frac{kr^2}{2f}\left(1 - \frac{\lambda^2}{\lambda_0^2}\right) - \frac{\mu(\lambda)Nr^2}{4R}\right]\right|^2 \tag{17}$$

where μ varies linearly with λ, b is the base thickness, q is the source-to-lens distance, Z is the number of zones, and g(λ) is the neutron spectrum. For 10% bandwidth, μ and g(λ) can be taken to be constant. The modulation transfer function can be calculated from the PSF, and we do this in the Phase II work plan for specific designs.

Sensitivity to zone step size

A tolerance estimate may be given for the step size for zone coherence by allowing a phase error of $\pm .05(2\pi)$. If the errors are random, this corresponds to a thickness error, Δt, equal to

$$\Delta t = \pm \frac{.05(2\pi)}{k\delta\sqrt{N}} = \pm\frac{.05\lambda}{\delta\sqrt{N}} \tag{18}$$

If the error is not random, then $\Delta t \sim 1/N$. For Teflon at 1.8 Å using 78 unit lenses (as for our Phase I experiments), the tolerance would be $\pm 0.38\mu m$.

Flux Transmission

The transmitted flux, W, normalized to the incident intensity, I_0, is

$$\frac{W}{I_0} = 2\pi \sum_{n=0}^{Z-1} \int_{\sqrt{\frac{naA^2}{8}}}^{\sqrt{\frac{(n+1)aA^2}{8}}} rdrExp\left[-\frac{8}{A^2} r^2 + an \right] = \pi \frac{A^2}{8} Z(1 - e^{-a}) \tag{19}$$

where A, is the absorption diameter for the parabolic lens. For a parabolic lens

$$\frac{W}{I_0} = 2\pi \int_0^{\infty} rdrExp\left[-\frac{8}{A^2} r^2 \right] = \pi \frac{A^2}{8} \tag{20}$$

Thus, the flux enhancement for the Fresnel lens over the parabola is

$$\text{Flux enhancement} = Z(1 - e^{-a}) \tag{21}$$

The flux incident on a Fresnel lens, W_{inc}, is

$$W_{inc} = I_0 \pi Z a \frac{A^2}{8} \tag{22}$$

Thus, the lens transmission, T_L, is

$$T_L = \frac{W}{W_{inc}} = \frac{1 - e^{-a}}{a} \tag{23}$$

Including base absorption, with base width b, the total transmission is

$$T = T_L e^{-\mu N b} = \frac{1 - e^{-a}}{a} e^{-\mu N b} \tag{24}$$

Aperture diameter for the Fresnel lens

$$\text{Aperture diameter} = D_Z = 2 r_Z = A\sqrt{\frac{Za}{2}} \tag{25}$$

Intensity Increase vs. Parabolic Lenses

The on-axis image intensity from a point source is given by *PSF(0)*. For a monochromatic source, the increase in intensity for a Fresnel lens over a parabolic lens, ρ, is given by

$$\rho = Z\left(1 - e^{-a/2}\right)^2 \tag{26}$$

for incoherence between zones and by

$$\rho = Z^2\left(1 - e^{-a/2}\right)^2 \tag{27}$$

for coherence between zones. From Eqs. (26) and (27) we see that the intensity enhancement increases with increasing a towards an asymptote of Z or Z^2.

Scattering on flat transitions between zones

One issue with Fresnel lenses of this type is that neutrons can be reflected from the surfaces of the lenses that are parallel to the principal axis. In addition, the corners of the steps can cause slit scattering. Neutrons may travel at sufficient angle to move from one zone to another as they pass through the multiple unit lenses in the CRL. In this case, some neutrons will strike the zone wall. For the larger inner zones, the cross section of the wall is negligible; however for thin outer zones, the probability of striking the wall will be larger. As an example, for a Teflon lens at 1.8 Å with N=100, a=.939, the zone wall height is 380μm, and, given a 1 *m* focal length and field of view of 2 *cm*, the maximum neutron angle through the lens is < 10 mrad. Thus, the wall dimension seen by the neutron is approximately 3.8μm. For Z=5, the outer zone size is 89μm. A neutron entering in the central region of the lens is unlikely to strike a

wall, but a neutron entering in the outer zone has greater than 50% probability of striking a wall. However, passing through the region of the wall may not be destructive. The critical angle for total reflection from teflon at 1.8Å is about 2 mrad, so that a range of neutrons striking a highly polished wall will be reflected. This can be avoided by not polishing the zone wall, in which case the neutron will pass through the wall relatively unaffected. Thus, we do not expect a significant loss of flux from neutrons striking the walls separating zones.

Alignment

While we originally expected the alignment of the Fresnel unit lenses relative to one another to require more accuracy than simple parabolic lenses, we have not found this to be true. If a neutron does not strike the steep wall between zones, it will refract just as for a parabolic lens. As shown in Adelphi's patent for Fresnel CRLs [17], ignoring losses to the walls, each zone must be about twice the median misalignment to preserve the transmitted intensity and resolution is not significantly affected by misalignment. Essentially, the effective aperture is reduced when there is random variation of the unit lenses off the average optical axis of the lenses, but that there is no other degradation to image quality or efficiency [14]. If those neutrons that do pass through the region of the walls are not scattered, then alignment will be no more critical than for the parabolic case. If scattering from the boundary walls is significant, then alignment should be on the order of the radial extent of the wall, something on the order of 10-20 μm.

Fresnel Type

We can manufacture two types of Fresnel lens. One possibility is a classic flat lens as shown in Fig.12(c). These are easy to stack and take up minimal space, but cutting accurate parabolic shapes between the steep walls can be challenging. Another possibility is to use a curved shape like that in Fig. 12(b) and simply cut the back from the parabolic lens in steps. This is easy to manufacture and would allow zones to be 10 *μm* wide or less using diamond tip machining. However, these lenses are more difficult to stack.

References

[1] J. T. Cremer, M. A. Piestrup, H. Park, C. K. Gary, R. H. Pantell, C. J. Glinka, J. G. Barker, "Imaging hydrogenous materials with a neutron microscope," Appl. Phys. Letts. **87**, Oct. 2005.

[2] J. T. Cremer, M. A. Piestrup, C. K. Gary, R. H. Pantell, and C. J. Glinka, "Biological Imaging with a Neutron Microscope", Appl. Phys. Lett. **85,** 494 (2004).

[3] H. R. Beguiristain, I. S. Anderson, C. D. Dewhurst, M. A. Piestrup, J. T. Cremer, and R. H. Pantell, "A simple neutron microscope using a compound refractive lens" Appl. Phys. Lett **81**, 4290-4292 (2002).

[4] DOE Phase II SBIR (DE-FG02-03ER83862), "An inexpensive, efficient Neutron Monochromator," J. T. Cremer, Principal Investigator, 6/27/03-6/26/05.

[5] H. Park, J. T. Cremer, M. A. Piestrup, C. K. Gary**,** Rex P. Hjelm, W.C.L.J. Sellyey, R. H. Pantell "Measured operational neutron energies of compound refractive lenses" Nuclear Inst. and Methods in Physics Research, B, **251,** 507 (2006).

[6] J. T. Cremer, H. Park, M. A. Piestrup, C. K. Gary, R. H. Pantell R. G. Flocchini, H. P. Egbert, M. D. Kloh, R. B. Walker, "A simple microscope using a compound refractive lens and a wide-bandwidth thermal neutron beam," Submitted to Appl. Phys. Lett. (Nov. 2006).

[7] A. Snigivrev, V. Kohn, I. Snigireva and B. Lengeler, "A compound refractive lens for focusing high-energy X-rays, Nature 384, 49 (1996).

[8] M. A. Piestrup, H. R. Beguiristain, C. K. Gary, J. T. Cremer, and R. H. Pantell "Two-dimensional x-ray focusing from compound lenses made of plastic," Rev.Scient. Instrum., **71**, 4375-4379(2000).

[9] Y. I. Dudchik, N. N. Kolchevsky, F. F. Komarov, M. A. Piestrup, J. T. Cremer, C. K. Gary, H. Park, and A. M. Khounsary, "Microspot x-ray focusing using a short focal-length compound refractive lenses," Rev. Sci. Instrum. **75**, 4651-4655 (2004).

[10] M. A. Piestrup, C. K. Gary, Y. I. Dudchik, N. N. Kolchevsky, F. F. Komarov, H. Park, J. T. Cremer, R.H. Pantell, "A microscope using an x-ray tube and a bubble compound refractive lens," Appl. Phys. Lett. **86**, (2005).

[11] H. R. Beguiristain, J. T. Cremer, M. A. Piestrup, C. K. Gary and R. H. Pantell, "X-ray focusing using compound lenses made of Beryllium," Optics Letters, **27**, 778-780 (2002).

[12] J. T. Cremer , M. A. Piestrup, H. R. Beguiristain, C. K. Gary, and R. H. Pantell, "Large aperture compound lenses made of lithium," Rev. Scient. Instrum. **74**, 2262, (2003).

[13] M. A. Piestrup, R. H. Pantell, J. T. Cremer and H. R. Beguiristain, "Compound Refractive Lens for X-rays," US Patent, 6,269,145 B1, Jul. 31, 2001

[14] R. H. Pantell, J. Feinstein, M. A. Piestrup, H. R. Beguiristain, C. K. Gary and J. T. Cremer, "The effect of unit lens alignment and surface quality on compound refractive lens performance," Rev. Scient. Instrum. **72**, 48 (2001).

[15] B. Lengeler, C.G. Schroer, M. Richwin, and J. Tummler, "A microscope for hard x-rays based on parabolic compound refractive lenses," Appl. Phys. Lett., **74**, (1999).

[16] Website for MCNPX is http://mcnpx.lanl.gov and MCNP 5 is http://laws.lanl.gov/x5/MCNP/index.html.

[17] W.M. Gibson, A. J. Schultz, H.H. Chen-Mayer, D.F.R. Mildner, T. Gnäupel-Herold, M.E. Miller, H.J. Prask, R. Vitt, R. Youngman, J.M. Carpenter, "Polycapillary focusing optic for small-sample neutron crystallography", J. Appl. Cryst., **35** 677(2002).

[18] Meyer-Arendt, J.R., *Introduction to Classical and Modern Optics, Prentice Hall, 1984.*

[19] ASTM Standard E2023-99, "Fabrication of Neutron Radiographic Sensitivity Indicators," ASTM International (2004).

[20] UC Davis Reactor Checks Firefighting Tanker equipment for US Forest Service, www.news.ucdavis.edu/search/printable_news.lasso?id+7774&table=news

[21] Glen MacGillivay, "Imaging with Neutrons: The Other Penetrating Radiation," Nray Services (Petawawa, ON, Canada), OE Reports, #198 (June 2000) www.spie.org/web/oer/june00/cover1.html

[22] A. Kapadia , C. E. Floyd, SPIE **5745**, 737 (2005).

[23] MIT Nuclear Reactor Lab, BNCT Facility, http://web.mit.edu/nrl/www/bnct/bnct_home.html

[24] NIST: X-Ray Mass Attenuation Coefficients – Table 2, compositions of various human tissues taken from ICRU Report 44 (1989), http://physics.nist.gov/PhysRefData/XrayMassCoef/tab2.html.

[25] M. R. Eskildsen, P. L. Gammel, E. D. Isaacs, C. Detlefs, K. Mortensen and D. J. Bishop, "Compound Refractive Optics for Imaging and Focusing of Low-Energy Neutrons," Nature **391**, 563 (1998).

[26] S.M. Choi, J.G. Barker, C.J. Glinka, Y.T. Cheng, and P.L. Gammel, "Focusing cold neutrons with cold neutrons with multiple biconcave lenses for small-angle neutron scattering", *J. Appl. Cryst.* (2000), **33**, 793-796

[27] D.F.R. Mildner, B. Hammouda, S.R. Kline, "A refractive focusing lens system for samll –angle neutron scattering", *J. Appl. Cryst.* (2005). **38**, 979-987M. A. Piestrup, X-ray and Neutron Imaging" US Patent # 6992313 (2006).

[28] I. Grillo, Soft-Matter Characterization, edited by Redouane Borsali, Robert Pecora, ISBN: 978-1-4020-8290-0, Vol 2, Ch. 13, April 2009

[29] Fuji Film Medical Systems USA, Inc., 419 West Avenue, Stamford, CT 06902, BAS-ND

[30] S. Tazaki, K. Neriishi, K. Takahashi, M. Etoh, Y. Karasawa, S. Kumazawa, N. Niimura, *Nucl. Instrum. Methods*, **A 424**, 20 (1999